RESEARCH LETTER
10.1029/2022GL100418

Key Points:

- The nucleation length of injection-induced laboratory earthquakes reduces with higher injection rate and greater effective normal stress
- Injection-induced laboratory earthquakes with smaller nucleation lengths exhibit higher peak slip rates and larger fault slip displacements
- Fast-rate fluid injection may cause initially stable fault patches of smaller sizes to slip seismically, leading to higher seismic hazards

Author Contributions:

Conceptualization: Yinlin Ji
Funding acquisition: Hannes Hofmann
Investigation: Yinlin Ji, Lei Wang
Methodology: Yinlin Ji
Software: Grzegorz Kwiatek
Writing – original draft: Yinlin Ji
Writing – review & editing: Yinlin Ji, Lei Wang, Hannes Hofmann, Grzegorz Kwiatek, Georg Dresen

High-Rate Fluid Injection Reduces the Nucleation Length of Laboratory Earthquakes on Critically Stressed Faults in Granite

Yinlin Ji[1] , Lei Wang[2] , Hannes Hofmann[1] , Grzegorz Kwiatek[2] , and Georg Dresen[2]

[1]Helmholtz Centre Potsdam GFZ German Research Centre for Geosciences, Section 4.8 Geoenergy, Potsdam, Germany, [2]Helmholtz Centre Potsdam GFZ German Research Centre for Geosciences, Section 4.2 Geomechanics and Scientific Drilling, Potsdam, Germany

Abstract We conducted fluid injection experiments on cylindrical low-permeability granite samples with a critically stressed sawcut fault at local injection rates of 0.2 and 0.8 mL/min and confining pressures of 31 and 61 MPa. A local array of six strain gauges attached close to the faults allows us to estimate the nucleation length of each injection-induced dynamic slip event (i.e., laboratory earthquake). We find nucleation lengths decrease from approximately 90% to <15% of the fault length with higher injection rate and increased effective normal stress. Injection-induced laboratory earthquakes with smaller nucleation lengths show generally higher peak slip rates and larger fault slip displacements, signifying an intensified seismic hazard. Our results also indicate that initially stable fault patches may be reactivated to slip seismically by increasing injection rates. This study systematically demonstrates that higher injection rates constitute dynamic loading, which increase the seismic hazard by shrinking the earthquake nucleation length.

Plain Language Summary Earthquakes associated with fluid injection in various geo-energy settings, such as shale gas and deep geothermal energy, have shelved many projects with great potential. However, the injection-rate dependence of earthquake nucleation length, which characterizes the length of a slowly slipping (creeping) fault patch in preparation for a subsequent earthquake, remains to be studied. To this end, we performed fluid injection experiments on low-permeability granite samples containing a critically stressed sawcut fault. We demonstrate that the nucleation length of injection-induced laboratory earthquakes shrinks with higher effective normal stress and larger injection rate. We show that laboratory earthquakes induced by higher fluid injection rates are characterized by smaller nucleation lengths, faster peak slip rates, and larger fault slip displacements. Our results also suggest that a stable fault patch subject to low-rate injection may be induced to slip seismically by increasing injection rates. Our findings may explain the higher seismic hazards associated with higher injection rates as has been frequently documented in field cases.

1. Introduction

Fluid injection into the subsurface is known to potentially induce seismic activity, sometimes including large-magnitude earthquakes (e.g., Eyre et al., 2019; Goebel, et al., 2017; Grigoli et al., 2018; Healy et al., 1968; Lei et al., 2017). Injection-induced seismicity poses major challenges to the exploitation of geo-resources, such as shale gas and deep geothermal energy (e.g., Ellsworth et al., 2016; Elsworth, 2013; Ji, Hofmann, et al., 2022; Zang et al., 2014). For a uniformly pressurized fault, fault reactivation is predicted by the Mohr-Coulomb failure criterion and the effective stress law (Terzaghi, 1923). The increase of fluid pressure (p) reduces the effective normal stress (σ_n') and thus the peak shear strength (τ_p) of the fault. Failure occurs when the shear strength is overcome by the resolved shear stress (τ) along the fault (e.g., Jaeger et al., 2009):

$$\tau \geq \tau_p = \mu \sigma_n' = \mu (\sigma_n - p) \tag{1}$$

where μ and σ_n are the friction coefficient and normal stress along the fault, respectively.

Industrial injection measures may induce large-magnitude earthquakes on large faults (Stein & Wysession, 2009; Zoback & Gorelick, 2012), where fluid pressure distribution is spatially and temporally heterogeneous. The Mohr-Coulomb failure criterion incorporating the effective stress law (Equation 1) may then only apply to estimating the critical stress at failure and slip initiation of local fault patches (e,g., Gischig, 2015; Ji & Wu, 2020;

Passelègue et al., 2018; Rutter & Hackston, 2017; Sáez et al., 2022). Fault reactivation induced by local fluid pressure perturbation has been reported over a wide range of spatial scales from lab (centimeters to meters), mine (decameters) to reservoir (kilometers) faults. In laboratory samples, fault slip induced by elevated and heterogeneous fluid pressure has been studied by regulating the injection rate, the prestresses applied to faults, and fault roughness (Cebry & McLaskey, 2021; Gori et al., 2021; Ji & Wu, 2020; Passelègue et al., 2018). Local fluid pressure perturbations due to fluid injection may directly induce aseismic slow slip, and then trigger seismic events, as has been observed for the induced seismic slip of a carbonate fault zone at mine scale in the Low Noise Underground Laboratory in France (Cappa et al., 2018, 2019; Guglielmi et al., 2015), and the 2016 M_w 4.1 earthquake initiated in the Duvernay shale's caprock at field scale in Canada (Eyre et al., 2019).

Investigating the nucleation phase of fault slip induced by local fluid pressure perturbations will advance our understanding of injection-induced seismicity, and potentially help identify seismic and/or aseismic precursors to unstable fault slip. The characterization of the nucleation process during laboratory earthquakes has been reported extensively. Ohnaka and Shen (1999) and Latour et al. (2013) found that nucleation preceding dynamic rupture propagation is composed of two distinct stages, that is, a first quasi-static stage and a subsequent acceleration stage. The length scale along which rupture propagation becomes unstable is defined as the nucleation length, which may vary depending on many intrinsic (e.g., fault heterogeneity) and extrinsic parameters (e.g., loading conditions) (Kaneko & Lapusta, 2008). In accordance with theoretical predictions (Ampuero & Rubin, 2008; Rubin & Ampuero, 2005), the directly measured nucleation length for dry samples is found to decrease with higher normal stress (Latour et al., 2013; McLaskey, 2019) and larger loading rate (Guérin-Marthe et al., 2019). Similarly, the nucleation length calculated from rate-and-state frictional parameters obtained from velocity-stepping tests on wet fault gouges under a variety of boundary conditions is smaller at lower fluid pressures and higher slip rates (Cappa et al., 2019). More recently, Gori et al. (2021) demonstrated for the first time that the nucleation length of laboratory earthquakes on plastic polymers induced by high-rate local fluid injection is smaller than that in the low-rate cases, suggesting that higher injection rates may constitute dynamic loading and reduce the nucleation length. However, a systematic laboratory study characterizing the injection-rate dependence of earthquake nucleation length of faults in rock samples and its implications for injection-induced seismicity are lacking.

In this study, we aimed to explore experimentally the dependence of injection-induced earthquake nucleation length on local injection rate and effective stress acting on critically stressed faults in granite. To this end, we injected fluid locally through a small borehole to critically stressed sawcut faults in low-permeability granite samples at different injection rates and confining pressures while monitoring the precursory local strain changes, macroscopic fault slip and acoustic emission (AE) activity. We estimated the nucleation length of slip events using either premonitory local shear stress changes along the fault estimated from strain gauge data or precursory AE hypocenter locations.

2. Materials and Methods

The granite sample used in this study was cored from Odenwald basement rocks in Rimbach, Germany. The granite is mainly composed of homogenously distributed quartz, feldspar, and mica with grain sizes ranging from 1 to 3 mm (Kluge et al., 2020). The initial porosity and permeability of the granite are as low as ~0.6% and ~1×10^{-18} m^2 (measured at a hydrostatic confining pressure of 2 MPa), respectively. The uniaxial compressive strength of the granite ranges from approximately 120–142 MPa (Blöcher et al., 2019). In this study, a cylindrical sample with a diameter of 50 mm was first cut and ground flat to a length of 100 mm. An elliptical fault was then prepared in the sample by cutting the cylinder at 30° to the sample axis. Fault surfaces of both sawcut blocks were polished using sandpaper with a grit size of 201 µm. A 1.8-mm-diameter borehole was drilled near the short edge of each sample half to allow direct fluid access to the fault surface (Figure 1a). Two samples were prepared following the same procedure to make sure that they have similar initial surface roughness. The low permeability and high strength of the granite ensure that the rock matrix remains nearly intact and impermeable and thus fluid flow is confined within the fault during the experiments (Ji et al., 2021).

Eight strain gauges were attached onto the sample surface to monitor the deformation of rock matrix and fault (Figure 1). The vertical deformation of the rock matrix was measured by two strain gauges (SV3 and SH4) glued close to the center of the upper and lower sample halves away from the fault (Figure 1b). The other six strain gauges (SGF1, SGF2, SGF3, SGF4, SGF5 and SGF6) were attached parallel to the sample axis and equally
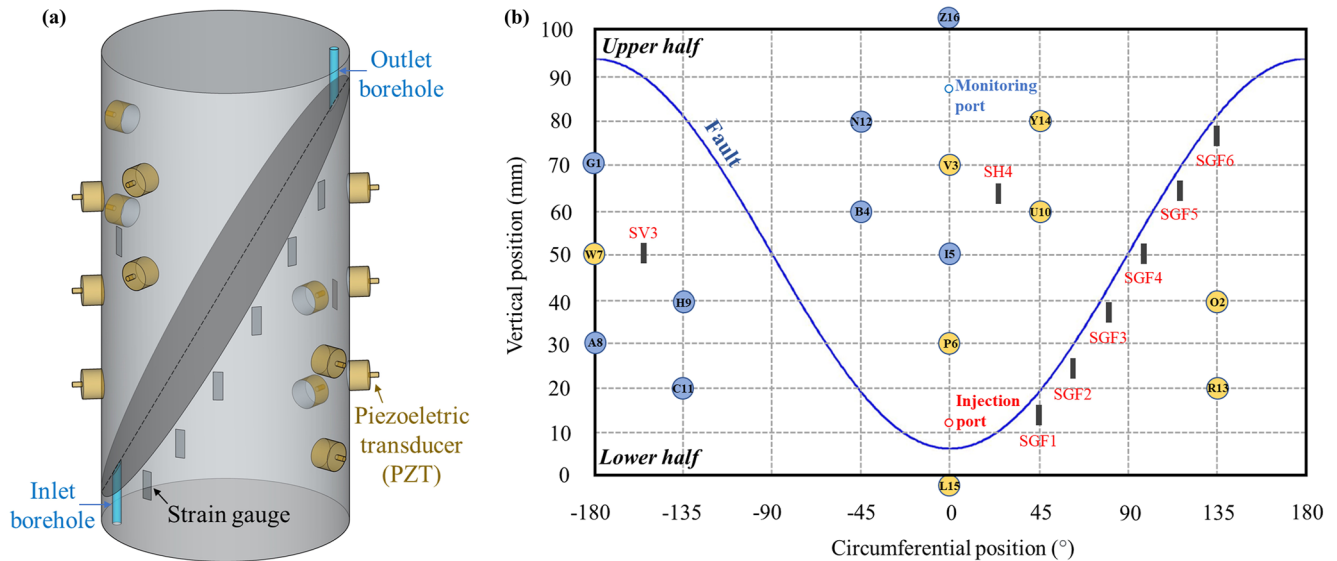
Figure 1. Experimental configuration. (a) Schematic drawing of the sample assembly. (b) Detailed sensor map showing the locations of injection and monitoring ports, strain gauges and piezoelectric transducers. The eight transducers (half of the total amount) labelled blue serve as ultrasonic transmitters to measure and update the ultrasonic *P*-wave velocities at 10 s time interval throughout the experiments. The two sensors L15 and Z16 mounted inside the steel endcaps are not shown in (a).

spaced along the fault between the circumferential positions 45° and 135°. These six strain gauges were located near the fault on the lower sample half, allowing us to calculate local fault stresses and estimate the nucleation length of unstable fault slip events. In the additional series of experiments, we used alternative locations of strain gauges to constrain the nucleation length (see Text S1 and Figure S1 in Supporting Information S1). Eight pairs of piezoelectric transducers (PZTs, resonance frequency ~1 MHz) embedded in brass housings were directly mounted to the sample surface to record AE events (Figure 1). AE signals were first amplified by 40 dB using preamplifiers with 100 kHz high-pass filters. Continuous waveforms were recorded at 10 MHz sampling rate with 16-bit amplitude resolution. AE hypocenters were located by automatic picking of *P*-wave onsets using the combined Akaike Information Criterion and a convolutional neural network (e.g., Ross et al., 2018) to obtain rough and then refined positions of *P*-wave onsets, respectively. The equivalent differential time method (e.g., Font et al., 2004) was applied to estimate hypocenter locations and the inverse problem was solved using grid search followed by simplex optimization techniques. To calculate phase travel times, we used a quasi-anisotropic velocity model composed of 5 horizontal layers and 1 vertical layer, as estimated from active ultrasonic transmission measurements performed every 10 s. This procedure allowed us to account for deformation-induced elastic anisotropy and changes in the velocity model. The average AE hypocenter location accuracy is ±2 mm (Stanchits et al., 2011).

The oven-dried samples and steel endcaps were jacketed in a neoprene sleeve and then placed in the MTS oil-medium triaxial cell. Samples were first subjected to 1 kPa vacuum. Subsequently the samples were fully saturated with distilled water at 2 MPa hydrostatic confining pressure and 0.2 MPa pore pressure. Prior to the experiments, all samples were preconditioned by cycling the confining pressure between 2 and 36 MPa to remove misalignment and plastic deformation (c. f., Ji, Kluge, et al., 2022; Kohli & Zoback, 2013).

On each sample we performed a series of fluid injection experiments. Two series of experiments were performed in this study, with the first at an initial shear stress (τ_c) of 85% peak shear strength (τ_p) and the second at 90% τ_p (Table S1 in Supporting Information S1). The first series of experiments (experiment series S1) were performed on the first sample consecutively. During the first fluid injection experiment S1-1 (Figure 2a), we measured the peak shear strength (τ_p) of the fault by advancing the axial piston at a constant rate of 1 µm/s at 31 MPa confining pressure and 1 MPa pore pressure (i.e., displacement-driven shear stage). We then reduced the shear stress to 85% of the peak shear strength by slowly retracting the axial piston. Subsequently, the axial piston was fixed, and the injection-driven shear stage was initiated by injecting distilled water from the bottom inlet borehole at an injection rate of 0.2 mL/min. Increasing pore pressure caused the critically stressed sawcut fault to slip and axial stress to relax at a fixed axial piston position. We terminated the experiment after two cycles of fast slip events
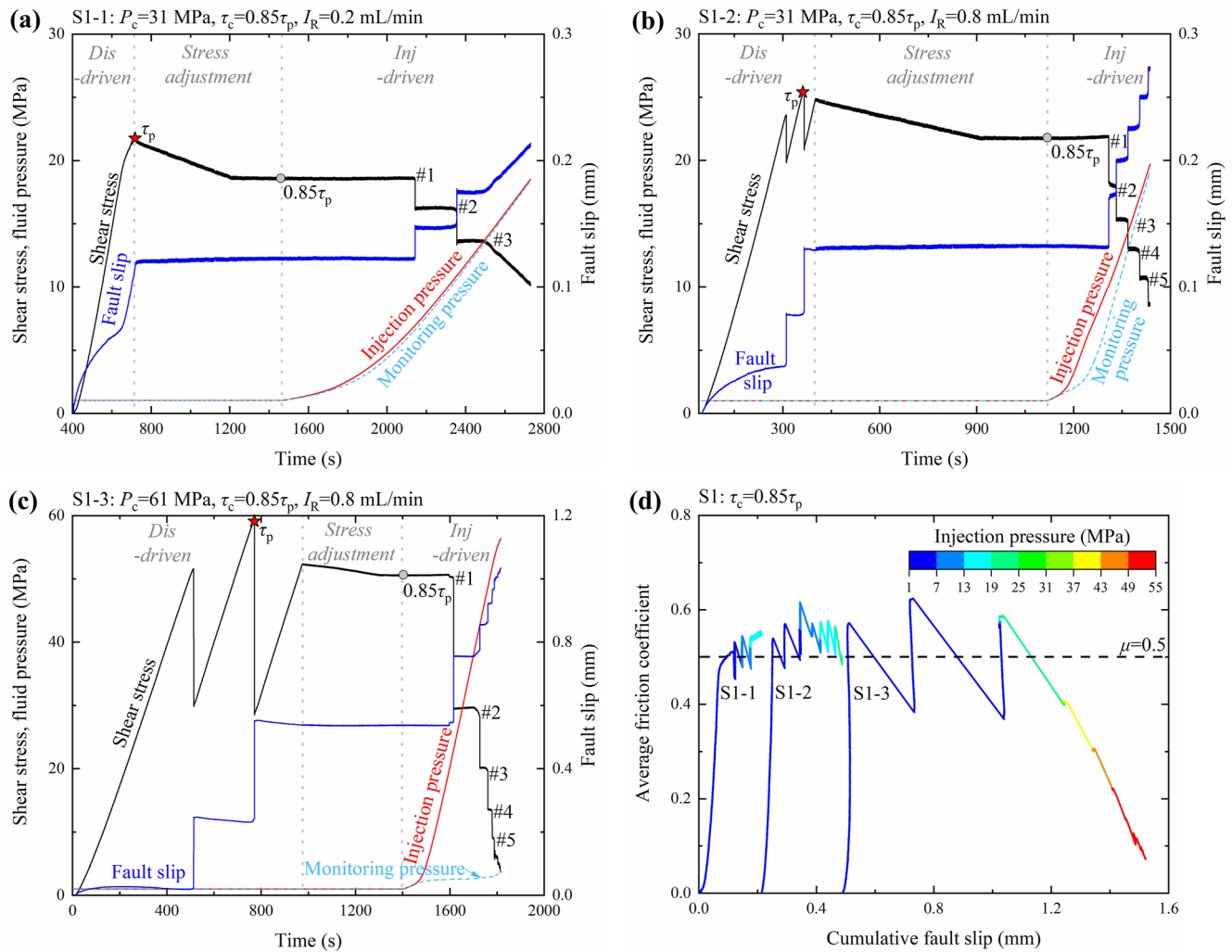
Figure 2. Time history of shear stress, fluid pressure and fault slip during the experiment (a) S1-1, (b) S1-2, (c) S1-3, as well as (d) average friction coefficient as a function of cumulative fault slip in the first series of experiments (color coded by the injection pressure). Each experiment is composed of three stages: displacement-driven shear stage, stress adjustment stage and injection-driven shear stage. P_c, τ_c, τ_p, I_R, μ are the confining pressure, initial shear stress, peak shear strength, injection rate, and friction coefficient, respectively.

and one slow slip event. Subsequently, the pore pressure was reduced to the initial value of 1 MPa and differential stress was reduced to zero (i.e., only hydrostatic pressure was applied) preparing for the ensuing experiments. A second fluid injection experiment S1-2 (Figure 2b) was conducted on the same sample at a higher injection rate of 0.8 mL/min using the same procedure at the same confining pressure of 31 MPa as in the first fluid injection experiment S1-1. We observed five episodes of rapid slip events before the termination of fluid injection. Afterward, the pore pressure was again reduced to the initial value of 1 MPa and the differential stress was removed, followed by the third fluid injection experiment S1-3 (Figure 2c) which was conducted at an injection rate of 0.8 mL/min and a confining pressure of 61 MPa. Additionally, we performed a second series of experiments (experiment series S2, see Table S1 in Supporting Information S1) including three fluid injection experiments, that is, S2-1, S2-2, and S2-3 (Figures S2a–S2c in Supporting Information S1), on another sample at a slightly higher initial shear stress of 90% τ_p following the same procedure as in the first series of experiments.

The axial stress was measured using an internal load cell with an accuracy of ±0.05 MPa. The external linear variable displacement transducer (outside the pressure vessel) was used to monitor the total axial displacement with an accuracy of ±0.5%. The fluid pressures in the inlet and outlet boreholes (i.e., injection and monitoring pressures, respectively) were recorded by the two pressure transducers of Quizix Q6000-20K pumps. Because fluid pumps, tubing and fluid itself provide additional compliance (e.g., Ji, Kluge, et al., 2022; Proctor et al., 2020), to

better compare the pressure responses and injected volume measurements in different experiments, the external dead volume was minimized and kept similar in the two series of experiments. The far-field average shear and normal stresses on the fault were resolved from axial stress and confining pressure, which were also corrected for the contact area reduction of the fault surface associated with fault slip (e.g., Ji, 2020; Ji & Wu, 2020; Tembe et al., 2010; Wang, Kwiatek, Rybacki, Bonnelye, et al., 2020). Sample shortening associated with fault slip was first calculated by subtracting the deformation of rock matrix and MTS testing system (stiffness of machine plus assembly ≈700 kN/mm) from the total axial displacement. Fault slip induced sample shortening was then projected to the principal fault slip direction to derive the fault slip displacement (Ji, 2020; Wang, Kwiatek, Rybacki, Bonnelye, et al., 2020). The mechanical deformation and hydraulic data were recorded simultaneously at 10 Hz. In addition, high-frequency (5,120 Hz) recordings of mechanical and deformation data were taken shortly before, during and after each dynamic fault slip event. After the experiments, we used the injection and monitoring pressures recorded during fluid injection to estimate the spatial-temporal evolution of fluid pressure on the fault surface using a finite element model (Ji et al., 2020) (Text S2 in Supporting Information S1).

3. Results

3.1. Fault Stability and AE Activity

3.1.1. Displacement-Driven Shear Stage

The temporal history of shear stress, fluid pressure (including injection and monitoring pressures), and fault slip during the fluid injection experiments performed at 85% peak shear strength (experiment series S1) is presented in Figures 2a–2c. At 31 MPa confining pressure and 1 MPa pore pressure, peak shear strengths (τ_p) of the fault were measured as 21.7 and 25.3 MPa in the displacement-driven shear stages in experiments S1-1 (Figure 2a) and S1-2 (Figure 2b), respectively. It is conceivable that the fault hardened with increasing slip displacement between experiments (e.g., Ji & Wu, 2020; Noël et al., 2019; Tembe et al., 2010). Displacement-driven sample behavior also differs markedly between the two experiments S1-1 and S1-2. In the first experiment S1-1, the sample showed a well-defined yield point at about 19.1 MPa shear stress, which was related to the onset of stable sliding along the sawcut fault. This is in contrast to the second experiment S1-2, which displayed two pronounced unstable stick-slip events with abrupt shear stress drops of about 3.7 and 4.5 MPa, respectively. The transition from stable sliding in the displacement-driven shear stage in the experiment S1-1 to unstable slip in S1-2 may be caused by increasing effective normal stress from 20.7 MPa in S1-1 to 24.6 MPa in S1-2 due to hardening. Besides, the dependence of fault frictional properties on cumulative slip displacement may have shifted the system toward unstable behavior (Text S3 in Supporting Information S1), as often observed in previous studies (e.g., Noël et al., 2019; Tinti et al., 2018). In the subsequent experiment S1-3 conducted at 61 MPa confining pressure and 1 MPa pore pressure, the fault strength was measured as 59.1 MPa during the displacement-driven shear stage, and the fault showed two stick-slip events with stress drops of 21.6 and 30.3 MPa, respectively. The displacement-driven shear stages in the second series of experiments (experiment series S2, Figures S2a–S2c in Supporting Information S1) exhibited similar behavior as above. The mechanical results are summarized in Table S1 in Supporting Information S1.

3.1.2. Injection-Driven Shear Stage

After the displacement-driven loading to peak shear strength, the shear stress was reduced to and stabilized at 85% (first experiment series S1) or 90% (second series S2) of the peak shear strength (corresponding to the stress adjustment stage in Figure 2a–2c and Figures S2a–S2c in Supporting Information S1, respectively). Subsequently, during the injection stage, we observed mostly stick-slip events (i.e., laboratory earthquakes exhibiting sudden macroscopic fault slip) with only two slow slip events (i.e., stable sliding) in the last stage of S1-1 and S2-2. Stick-slip instabilities and slow slip behavior have been reported in many previous laboratory studies on fault slip depending on weakening rate of the fault (fault stiffness) and unloading rate of the loading system (system stiffness) (Ji & Wu, 2020; Rice, 1983; Ruina, 1983). We estimated the stiffnesses of fault and system in terms of shear stress versus deformation along the principal fault slip direction (Text S3 in Supporting Information S1). In our study, the fault stiffness in stick-slip events was estimated from 95.7 to 132.1 MPa/mm (Figure S3 in Supporting Information S1) and larger than the system stiffness ranging from 85.9 to 92.8 MPa/mm (Text S3 and Table S1 in Supporting Information S1), in agreement with the observed unstable fault behavior (Rice, 1983; Ruina, 1983). As expected, the fault stiffness (55.8 to 91.5 MPa/mm) in slow slip events was generally smaller

than the system stiffness (85.9 to 92.8 MPa/mm). Note that a sampling rate of 5,120 Hz used in this study may lead to underestimated peak slip rates (c. f., Ohnaka & Shen, 1999; McLaskey & Yamashita, 2017; Xu et al., 2018); however, relative magnitudes of peak slip rate were captured. Peak slip rates of injection-induced stick-slip events estimated from sample shortening ranged from 1.3 to 319.1 mm/s (Table S1 in Supporting Information S1). It is generally larger for higher injection rates and larger confining pressures (Figure S4a and Table S1 in Supporting Information S1). Peak slip rates decreased significantly with progressive slip events (Figure S4a in Supporting Information S1), in agreement with the progressive decrease of shear and normal stresses at the onset of fault failure (c. f., Passelègue et al., 2020).

3.1.3. AE Activity During Fluid Injection

Fault slip induced by fluid injection produced very limited AE activity (cumulative AE number < 20) at 31 MPa confining pressure, while abundant AE events (cumulative AE number >250) were recorded at 61 MPa (Figures S5 and S6 in Supporting Information S1). The small number of AEs from our experiments at the low confining pressure of 31 MPa is possibly due to the combined effect of low effective stress on the smooth sawcut surface with the presence of water. Most AEs resulting from fluid injection were spatially distributed over the fault plane given the hypocenter location accuracy of ±2 mm (Figure S5 in Supporting Information S1). The injection-induced stable sliding of the fault in the later stage of S1-1 and S2-2 did not produce detectable AE events (Figure S6 in Supporting Information S1). In contrast, the cumulative number of AEs jumped with each rapid fault slip event, except the fourth and fifth stick-slip events in S1-2, presumably due to the smaller amount of stored elastic strain energy at the onset of these two later events (Passelègue et al., 2020). The increase of cumulative number of AEs generally decreased with progressive slip (Figure S6 in Supporting Information S1), positively related to the decreasing peak slip rate and fault slip displacement of dynamic slip events (Figure S4 in Supporting Information S1). The observed larger peak slip rates and fault slip displacements of dynamic fault slip events at higher injection rates (Figure S4 in Supporting Information S1) correspond to larger increases in cumulative number of AEs compared to the low injection rates (Figure S6 in Supporting Information S1). This agrees well with the findings from past studies that higher injection rates or faster pressurization may enhance the seismic activity regardless of fault drainage conditions (e.g., Ji & Wu, 2020; Ji, Hofmann et al., 2022; Passelègue et al., 2018; Wang, Kwiatek, Rybacki, Bohnhoff, & Dresen, 2020; Wang, Kwiatek, Rybacki, Bonnelye et al., 2020). Moreover, in contrast to the quiescence before and after the injection-induced stick-slip events at 31 MPa confining pressure, preparatory fault slip and post-failure stage at 61 MPa confining pressure were associated with AE activity, which is mainly due to small slip induced asperity damages, consistent with previous studies on sawcut surfaces in granite at high confining pressures (c. f., Dresen et al., 2020; Goebel, Kwiatek et al., 2017; Kwiatek, Goebel et al., 2014).

3.2. Friction Coefficient Evolution

We observed a difference between injection and monitoring pressures (Figure 2a–2c and Figures S2a–S2c in Supporting Information S1) especially for high-rate injections at higher confining pressures. The pressure difference indicates heterogeneous fluid pressure distribution on the fault surface. Fluid pressure distribution during fluid injection was modeled numerically (see Test S2, Figure S7, and Table S2 in Supporting Information S1). We quantified the degree of fluid pressure heterogeneity using the standard deviation of fluid pressures on the entire fault surface (see Equation S2 in Text S2 in Supporting Information S1), which increases with higher injection rate and greater effective stress (Table S1 in Supporting Information S1). This observation agrees well with previous studies (e.g., Ji et al., 2020; Passelègue et al., 2018; Rutter & Hackston, 2017). The nonuniform fluid pressure distribution may cause heterogeneous stress and friction across the fault. The average effective normal stress is the difference between average normal stress and average fluid pressure derived from the numerical model. The ratio of average shear stress and average effective normal stress is the average friction coefficient, which changed with cumulative fault slip (see Figure 2d and Figure S2d in Supporting Information S1). In the fluid injection experiments performed at 31 MPa confining pressure, the average friction coefficient was generally between 0.5 and 0.8 with some fluctuations, roughly consistent with Byerlee's rule for rock friction (Byerlee, 1978). In contrast, with increasing injection-driven fault slip displacement, the average friction coefficient at 61 MPa reduced dramatically to ~0.07 and ~0.3 in the first (Figure 2d) and second (Figure S2d in Supporting Information S1) series of experiments, respectively, suggesting additional fault weakening processes (see discussion in Section 4.1).
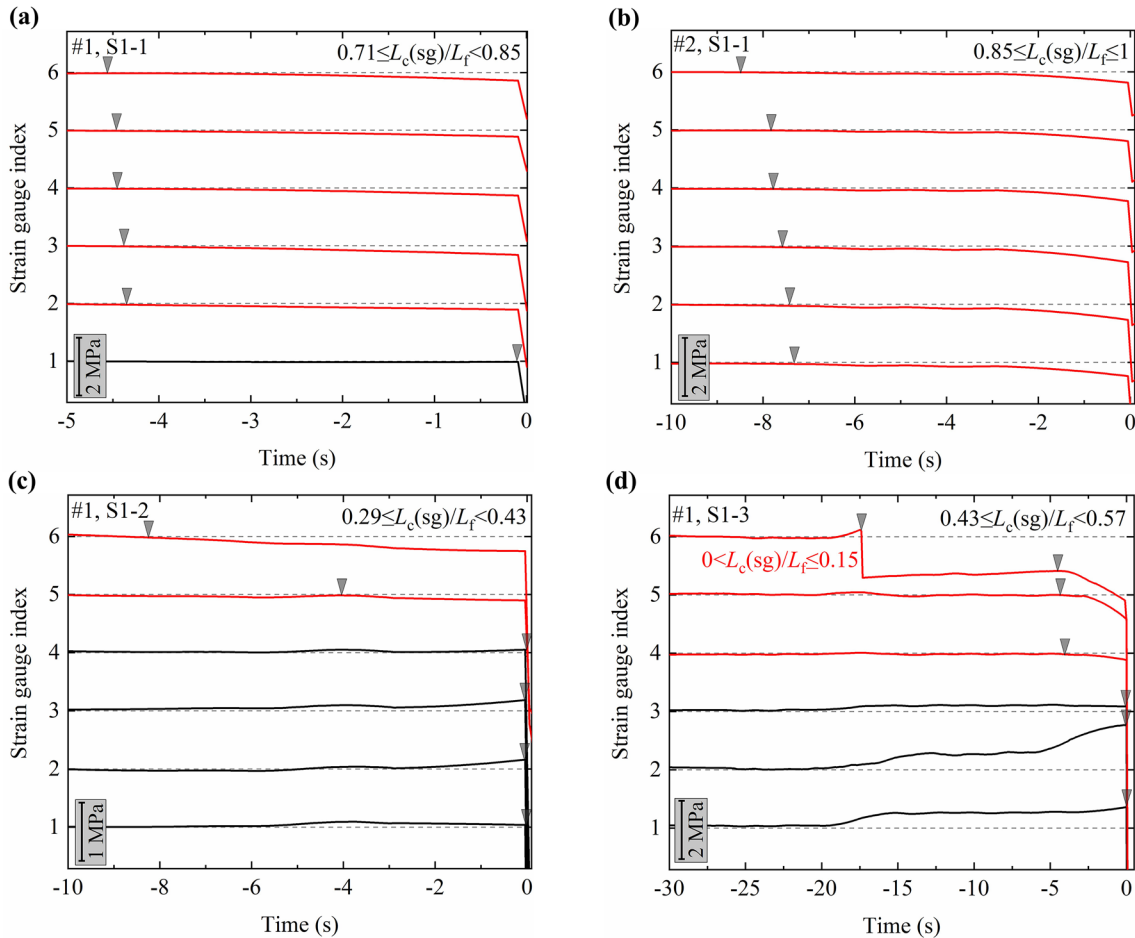
Figure 3. Estimation of the dimensionless nucleation length L_c(sg)/L_f, that is, measured nucleation length L_c(sg) using strain gauge data divided by fault length $L_f = 100$ mm, in the (a) first event in S1-1, (b) second event in S1-1, (c) first event in S1-2, and (d) first event in S1-3. Strain gauge data were filtered with a Savitzky-Golay filter to remove high-frequency noise. The strain gauge index increases from 1 to 6 toward the sample top (i.e., SGF1–SGF6). Time is offset at zero, corresponding to the time of rapid fault slip in each event. Gray triangles indicate the time of local slip initiation. The scale bars indicate the magnitude of shear stress change. Local shear stress experiencing premonitory drop and indicating local patch creeping is displayed in red, while others beyond the creeping patch is displayed in black. Starting from the fault upper end (i.e., from strain gauge #6 to #1), the last strain gauge displayed in red and the first strain gauge in black define the lower and upper bounds of the nucleation length, respectively. The first macroscopic dynamic slip event in S1-3 occurred following a contained rupture near strain gauge #6 showing a local shear stress drop of ~1.5 MPa.

3.3. Nucleation Length of Injection-Induced Laboratory Earthquakes

In the present study, the nucleation length of the laboratory earthquakes induced by fluid injection was estimated from the local axial strain changes (converted to stress), which were recorded by the six local axial strain gauges placed along the sawcut fault (see Figure 1). Particularly, the local axial strain change was converted to local shear stress change (Passelègue et al., 2016, 2020) assuming a constant Young's modulus of rock matrix estimated from the respective displacement-driven shear stage in each experiment (Text S4 and Figure S8 in Supporting Information S1). Here the transient change of confining pressure was assumed to be minor during fault slip events due to the relatively high compliance of the confining system (Acosta et al., 2018; Passelègue et al., 2016, 2020), and thus a constant Young's modulus of rock matrix was used to estimate the local shear stress.

We estimated the nucleation length from the temporal evolution of local shear stresses converted from local axial strains prior to dynamic slip events (Figure 3). The strain gauges are labeled from one to six toward the sample top (i.e., SGF1 to SGF6, see Figure 1). High-frequency noise in the strain gauge data was removed using a Savitzky-Golay filter. In our experimental configuration, the rupture propagation could be a complex mixture of in-plane rupture (mode II) along the fault length and anti-plane rupture (mode III) along the fault width (Passelègue et al., 2016). However, in order to estimate the nucleation length, we projected the 2D elliptical fault

(50 mm by 100 mm) to the principal fault slip direction with a 1D fault length of 100 mm (i.e., long axis of the fault). The distance between two adjacent strain gauges is about 14 mm projected along the long axis of the fault. Before the fast (dynamic) slip event (time offset at zero in Figure 3), noticeable premonitory drops in local shear stresses (displayed in red in Figure 3) were observed in the creeping patch while the local shear stress increased or remained almost unchanged beyond it (displayed in black). The gray arrows denote the time when local slip (local shear stress drop) initiated.

Our results demonstrate that slip nucleation sites were always near the sample top with nucleation lengths independent of the nucleation site (see Text S5 and Figure S9 in Supporting Information S1 for more details). The length of the creeping patch preceding dynamic slip event is understood as the nucleation length for a slip instability (Kaneko & Lapusta, 2008). Therefore, starting from the fault upper end (i.e., from strain gauge #6 to #1, Figure 3), the last strain gauge displayed in red (creeping), and the first strain gauge in black (locked) define the lower and upper bounds of the nucleation length, respectively. The estimation of nucleation length from the strain gauge data is not affected significantly by potential errors in determining local slip onset, since nucleation length is defined solely by strain gauges displaying premonitory stress drops. The ratio of nucleation length to fault dimension is found to affect fault slip dynamics (e.g., Cattania, 2019), and thus we obtained the dimensionless nucleation length $L_c(sg)/L_f$, which is the measured nucleation length $L_c(sg)$ using strain gauges divided by the fault length ($L_f = 100$ mm). For example, $L_c(sg)/L_f$ ratios of the first (Figure 3a) and second (Figure 3b) events in experiment S1-1 are about 0.71–0.85, and 0.85–1, respectively. The larger $L_c(sg)/L_f$ in the second event is likely due to the reduced effective normal stress. For the first event of experiment S1-2, we estimated $0.29 \leq L_c(sg)/L_f < 0.43$ (Figure 3c), which is smaller compared to the first event in S1-1 (0.71–0.85, Figure 3a) possibly caused by the higher injection rate used in S1-2 at otherwise similar stress conditions. Interestingly, after increasing the confining pressure to 61 MPa, a local shear stress drop of ~1.5 MPa near the sample top was captured by strain gauge #6 before the first injection-induced macroscopic dynamic slip event at time zero (Figure 3d), indicating a contained rupture with $0 < L_c(sg)/L_f \leq 0.15$. A similar contained rupture was again observed in the third experiment S2-3 (Figure S10c in Supporting Information S1) of the second series of experiments. Injection-induced contained ruptures have been previously reported in laboratory studies on much larger faults (40 cm by 200 cm) in granite (Lockner et al., 1982). Our estimates of dimensionless nucleation lengths determined by the strain gauge data are supported by results obtained from 2D spreading of AE clusters (Text S6 and Figure S11 in Supporting Information S1).

4. Discussion

4.1. Nucleation Process of Injection-Induced Laboratory Earthquakes

The two nucleation phases from quasistatic to accelerating slip as described in many previous studies (e.g., Latour et al., 2013; Ohnaka & Shen, 1999) were not well resolved by the strain gauge array before the injection-induced dynamic slip events at 31 MPa confining pressure (Figures 3a–3c). We attribute this to a mixed-mode (mode II and mode III) rupture propagation associated with the fault geometry (Passelègue et al., 2016), which differs from the mode II rupture propagation along a long fault with a narrow width as often used in previous studies (e.g., Guérin-Marthe et al., 2019; Latour et al., 2013; McLaskey, 2019; McLaskey & Yamashita, 2017; Ohnaka & Shen, 1999; Xu et al., 2018). Unlike the experiments at 31 MPa confining pressure, the events at 61 MPa were preceded by much more pronounced premonitory local shear stress drops (>0.2 MPa/s) in the creeping patches observed in the first (see strain gauges #5 and #6 in Figure 3d) and second (see strain gauges #2–#6 in Figure S12 in Supporting Information S1) events in the experiment S1-3. For the second event in S1-3 (Figure S12 in Supporting Information S1), the precursory local shear stress drops initiate much earlier associated with an apparent quasistatic rupture velocity of about 2.9 mm/s. Our strain gauge array only allows us to estimate an apparent rupture velocity, which may differ from the true value due to the mixed-mode 2D rupture propagation across the elliptical fault. Such quasistatic rupture propagation with pronounced local shear stress drops in the creeping patches was also well monitored before later injection-induced stick-slip events at 61 MPa confining pressure.

The quasistatic rupture propagation at the later stage of fluid injection at 61 MPa confining pressure indicates that the slowly expanding rupture area reached the outer boundary of the fault and induced local shear stress drops detectable by local strain gauges attached to the sample outer surface. This agrees with a broader distribution of AE events (Figure S5 in Supporting Information S1). Slip at 61 MPa confining pressure may be mainly caused by additional weakening mechanisms at the high confining pressure, which may result in rapid reduction of average
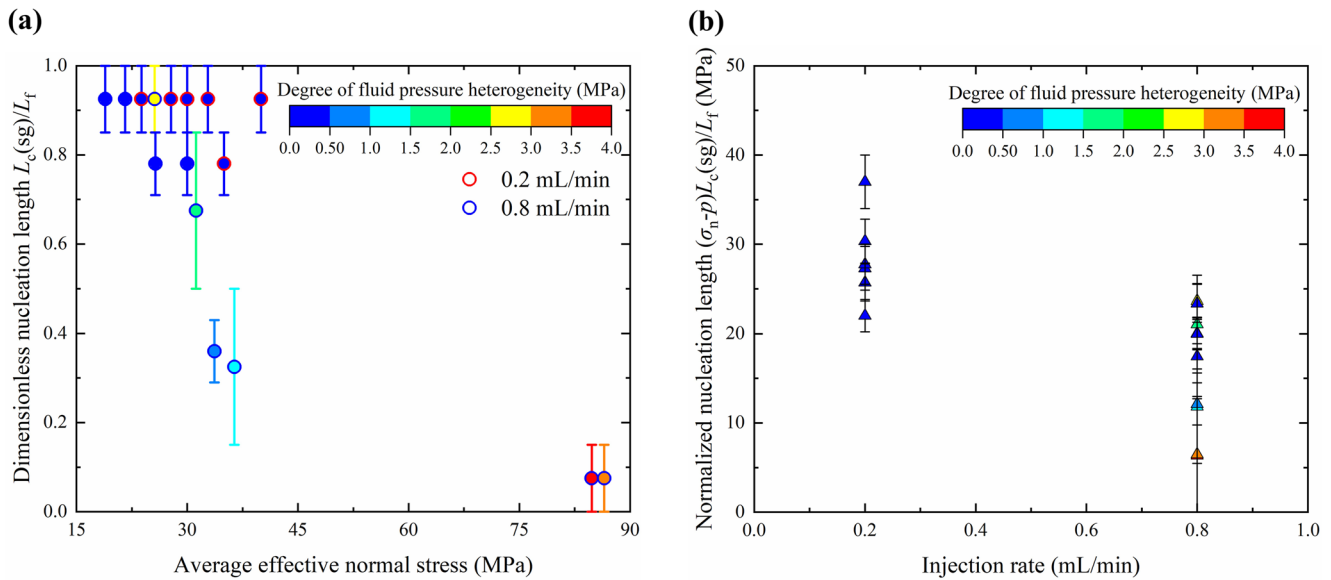
Figure 4. Nucleation length is affected by average effective normal stress and injection rate. (a) Dimensionless nucleation length $L_c(sg)/L_f$ as a function of average effective normal stress, and (b) normalized nucleation length $(\sigma_n-p)L_c(sg)/L_f$ as a function of injection rate. $L_c(sg)$ is the nucleation length measured by strain gauges; L_f is the fault length (100 mm); and σ_n-p is the average effective normal stress. The error bar is defined by the distance between two adjacent strain gauges projected along the long axis of fault. The data from two series of experiments are compiled in this figure and show that the nucleation length shrinks with greater average effective normal stress and higher injection rate. The data points are color coded by the degree of fluid pressure heterogeneity upon fault reactivation, which is quantified by the standard deviation of fluid pressure over the fault surface derived from the numerical model (Equation S2 in Text S2 in Supporting Information S1). Injection-induced earthquakes with smaller nucleation lengths are characterized by higher degrees of fluid pressure heterogeneity (also see Figure S14 in Supporting Information S1), indicating that localized fluid pressure perturbation may have induced the earthquake nucleation over smaller sizes.

friction during the later stage of fluid injection (Figure 2d and Figure S2d in Supporting Information S1). We examined the fault surface morphology before and after the second series of experiments and found that the root mean square asperity height was reduced by 20 μm, suggesting asperity damage after the experiments (Figures S13a and S13b in Supporting Information S1). Our AE results indicate that the asperity damage at 61 MPa confining pressure is more severe compared to the experiments at 31 MPa. Possibly gouge material resulting from severe asperity damage associated with surface smoothing may have contributed to powder lubrication at 61 MPa confining pressure (e.g., McLaskey & Lockner, 2014; Reches & Lockner, 2010). Importantly, we also identified melt structures on the fault surface after the first series of experiments (Figures S13c and S13d in Supporting Information S1), suggesting that melting and thermal pressurization (e.g., Acosta et al., 2018) may have also contributed to the observed dramatic weakening of the fault at 61 MPa. The effect of these additional weakening mechanisms on the nucleation process needs to be systematically studied in future work, which likely requires resolving the nucleation process in more detail. Nonetheless, we successfully estimated the nucleation length as the length of the fault patch experiencing premonitory slip right before a dynamic slip event (Kaneko & Lapusta, 2008).

4.2. Injection-Rate Dependence of Nucleation Length

We evaluate the controlling factors on the nucleation length of injection-induced laboratory earthquakes by summarizing the results of all experiments. Because of the significant drop of average friction coefficient at 61 MPa confining pressure with continuing fault slip, we exclude most of the results obtained from experiments performed at 61 MPa, while the two contained ruptures before the first injection-induced macroscopic dynamic slip events are included since the average friction coefficients upon rupturing are still compatible with Byerlee's rule (Byerlee, 1978). As shown in Figure 4a, the dimensionless nucleation length $L_c(sg)/L_f$, that is, measured nucleation length $L_c(sg)$ using strain gauges divided by fault length $L_f = 100$ mm, decreases significantly from ~0.9 to <0.15 as average effective normal stress increases from ~19 to ~87 MPa (Figure 4a). This is in good agreement with theoretical predictions (e.g., Ampuero & Rubin, 2008; Rubin & Ampuero, 2005) and previous experimental results (e.g., Latour et al., 2013; McLaskey, 2019). Because of this inverse dependence of

dimensionless nucleation length on effective normal stress and in order to assess the injection-rate dependence of nucleation length, we plot the normalized nucleation length $(\sigma_n - p)L_c(\text{sg})/L_f$, that is, the product of average effective normal stress $(\sigma_n - p)$ and dimensionless nucleation length $L_c (\text{sg})/L_f$ (Guérin-Marthe et al., 2019), as a function of injection rate. The normalized nucleation length $(\sigma_n - p)L_c(\text{sg})/L_f$ reduces significantly with higher injection rate (Figure 4b). This observation is similar to the effect of loading rates in displacement-driven shear friction experiments (Guérin-Marthe et al., 2019; Xu et al., 2018). We find that the events showing smaller nucleation lengths often occur at higher degrees of fluid pressure heterogeneity (Figure 4 and Figure S14 in Supporting Information S1, also see Equation S2 in Text S2 in Supporting Information S1). Both smaller nucleation length and higher degree of fluid pressure heterogeneity are favored by higher injection rate and greater effective normal stress. Therefore, it is conceivable that the stress heterogeneity caused by local fluid pressure perturbation may have caused nucleation of injection-induced laboratory earthquakes over smaller fault patches. More specifically, the local fluid pressure perturbation may have induced the spatio-temporally varying rate-and-state frictional parameters during fluid pressure diffusion (Cappa et al., 2019; Ji et al., 2020), affecting the nucleation length. However, we would expect the injection rate effect to be smaller for a high-permeability fault, where fluid pressure reaches equilibrium rapidly (Wang, Kwiatek, Rybacki, Bohnhoff, & Dresen, 2020, Wang, Kwiatek, Rybacki, Bonnelye et al., 2020).

We also compare the measured nucleation length with theoretical predictions. In addition to the quasistatic critical nucleation length $L_{b-a} = Gd_c/[(b-a)(\sigma_n - p)]$ (Scholz, 2019), the critical nucleation length could shrink to a minimum dynamic value $L_b = Gd_c/[b(\sigma_n - p)]$ in a fast nucleation process (Rubin & Ampuero, 2005). To constrain $(\sigma_n - p)L_{b-a}$ and $(\sigma_n - p)L_b$, we take shear modulus G as 31.3 GPa for Odenwald granite, characteristic length d_c as 1 μm, friction evolution parameter b as 0.028 and friction rate parameter $b-a$ as 0.004 for bare sawcut surface of granite faults (Marone et al., 1990; McLaskey & Yamashita, 2017). Further, we estimate the normalized nucleation lengths $(\sigma_n - p)L_b/L_f$ and $(\sigma_n - p)L_{b-a}/L_f$ as ~11.2 and ~78.3 MPa, respectively, roughly consistent with our laboratory measurements ranging from 6.5 to 37.0 MPa. Our laboratory measurements of nucleation lengths using strain gauges agree with theoretical predictions within one order of magnitude.

4.3. Implications for Injection-Induced Seismicity

Our results clearly demonstrate that the nucleation lengths of injection-induced stick-slip events along sawcut faults in granite reduce with higher effective normal stress and higher injection rate, within experimental uncertainties (Figure 4). The observed reduction in nucleation length with higher injection rate in this study may help to explain higher seismic hazards at enhanced fluid injection rates and/or faster pressurization as observed in field projects (e.g., Cuenot et al., 2008; Goebel & Shirzaei, 2020; Healy et al., 1968; Kwiatek et al., 2019; Langenbruch & Zoback, 2016; Weingarten et al., 2015), analytical/numerical modeling (e.g., Alghannam & Juanes, 2020; Rudnicki & Zhan, 2020), and laboratory experiments (e.g., Ji & Wu, 2020; Passelègue et al., 2018; Wang, Kwiatek, Rybacki, Bohnhoff, & Dresen, 2020, Wang, Kwiatek, Rybacki, Bonnelye et al., 2020). With the reduction of nucleation length, the peak slip rates during dynamic slip become larger, and the resulting fault slip displacements also increase given the same injected fluid volume (Figure S4 in Supporting Information S1). Fault patches may be stable at low fluid injection rates if critical nucleation sizes are larger than the seismogenic patch sizes. However, the slip of these smaller-sized fault patches could accelerate up to seismic velocities if the operational fluid injection rate is increased, resulting in injection-induced seismic events. Therefore, higher injection rates may increase the injection-induced seismic hazard by promoting the transition from aseismic to seismic slip and causing events with larger magnitudes. Our results thus highlight the role of injection rate on regulating injection-induced seismicity in addition to injected fluid volume (McGarr, 2014; McGarr & Barbour, 2018).

The data presented here may suggest that for a given fracture network, fluid injection rates could be optimized to enhance the permeability while maintaining large nucleation lengths and thus promote aseismic slip. More specifically, fracture/fault permeability in granitic rocks may be enhanced by self-propping of asperities accompanying increasing shear displacement, that is, shear stimulation (e.g., Ye & Ghassemi, 2018), and such self-propping shear process could be achieved aseismically by adjusting fluid injection rates. Practically, near real-time high-resolution seismic monitoring (Kwiatek et al., 2019) and implementation of an auto-adjustment procedure may help to limit seismic hazards during hydraulic stimulation.

5. Conclusions

We explored the dependence of nucleation length of laboratory earthquakes on fluid injection rate by conducting fluid injection experiments on critically stressed sawcut faults in low-permeability granite samples at different local injection rates and confining pressures. An array of local strain gauges and AE hypocenter locations were used to monitor the precursory slip of critically stressed faults in granite before injection-induced stick-slip failure. A smaller nucleation length associated with larger injection rates at higher effective normal stresses has been systematically observed, suggesting that high-rate fluid injection constitutes dynamic loading. Particularly, we find that the injection-induced slip events characterized by smaller nucleation lengths exhibit higher peak slip rates and larger fault slip displacements. Our results may also suggest that smaller-sized fault patches could be promoted to slip seismically at higher fluid injection rates. Our data provide plausible explanations for the causal link between higher fluid injection rates and higher seismic hazards in the presence of critically stressed large faults.

Data Availability Statement

This manuscript is accompanied by Supporting Information S1. The experimental data presented in this study are available at GFZ Data Services online: https://doi.org/10.5880/GFZ.4.8.2022.011.

References

Acosta, M., Passelègue, F. X., Schubnel, A., & Violay, M. (2018). Dynamic weakening during earthquakes controlled by fluid thermodynamics. *Nature Communications*, *9*(1), 3074. https://doi.org/10.1038/s41467-018-05603-9

Alghannam, M., & Juanes, R. (2020). Understanding rate effects in injection-induced earthquakes. *Nature Communications*, *11*(1), 3053. https://doi.org/10.1038/s41467-020-16860-y

Ampuero, J. P., & Rubin, A. M. (2008). Earthquake nucleation on rate and state faults-Aging and slip laws. *Journal of Geophysical Research*, *113*(B1), B01302. https://doi.org/10.1029/2007JB005082

Blöcher, G., Kluge, C., Goense, T., Pei, L., Bakker, R., & Bruhn, D. (2019). Hydraulic-mechanical characterization of geothermal reservoir rocks. In *Paper presented at the European geothermal congress*.

Byerlee, J. D. (1978). Friction of rocks. *Pure and Applied Geophysics*, *116*(4), 615–626. https://doi.org/10.1007/bf00876528

Cappa, F., Guglielmi, Y., Nussbaum, C., & Birkholzer, J. (2018). On the relationship between fault permeability increases, induced stress perturbation and the growth of aseismic slip during fluid injection. *Geophysical Research Letters*, *45*(20), 11–012. https://doi.org/10.1029/2018gl080233

Cappa, F., Scuderi, M. M., Collettini, C., Guglielmi, Y., & Avouac, J.-P. (2019). Stabilization of fault slip by fluid injection in the laboratory and in situ. *Science Advances*, *5*(3), eaau4065. https://doi.org/10.1126/sciadv.aau4065

Cattania, C. (2019). Complex earthquake sequences on simple faults. *Geophysical Research Letters*, *46*(17–18), 10384–10393. https://doi.org/10.1029/2019gl083628

Cebry, S. B. L., & McLaskey, G. C. (2021). Seismic swarms produced by rapid fluid injection into a low permeability laboratory fault. *Earth and Planetary Science Letters*, *557*, 116726. https://doi.org/10.1016/j.epsl.2020.116726

Cuenot, N., Dorbath, C., & Dorbath, L. (2008). Analysis of the microseismicity induced by fluid injections at the EGS site of soultz-sous-forêts (Alsace, France): Implications for the characterization of the geothermal reservoir properties. *Pure and Applied Geophysics*, *165*(5), 797–828. https://doi.org/10.1007/s00024-008-0335-7

Dresen, G., Kwiatek, G., Goebel, T., & Ben-Zion, Y. (2020). Seismic and aseismic preparatory processes before large stick–slip failure. *Pure and Applied Geophysics*, *177*(12), 1–20. https://doi.org/10.1007/s00024-020-02605-x

Ellsworth, W. L. (2013). Injection-Induced earthquakes. *Science*, *341*(6142), 1225942. https://doi.org/10.1126/science.1225942

Elsworth, D., Spiers, C. J., & Niemeijer, A. R. (2016). Understanding induced seismicity. *Science*, *354*(6318), 1380–1381. https://doi.org/10.1126/science.aal2584

Eyre, T. S., Eaton, D. W., Garagash, D. I., Zecevic, M., Venieri, M., Weir, R., & Lawton, D. C. (2019). The role of aseismic slip in hydraulic fracturing–induced seismicity. *Science Advances*, *5*(8), eaav7172. https://doi.org/10.1126/sciadv.aav7172

Font, Y., Kao, H., Lallemand, S., Liu, C.-S., & Chiao, L.-Y. (2004). Hypocentre determination offshore of eastern Taiwan using the maximum intersection method. *Geophysical Journal International*, *158*(2), 655–675. https://doi.org/10.1111/j.1365-246X.2004.02317.x

Gischig, V. S. (2015). Rupture propagation behavior and the largest possible earthquake induced by fluid injection into deep reservoirs. *Geophysical Research Letters*, *42*(18), 7420–7428. https://doi.org/10.1002/2015gl065072

Goebel, T. H. W., Kwiatek, G., Becker, T. W., Brodsky, E. E., & Dresen, G. (2017). What allows seismic events to grow big?: Insights from b-value and fault roughness analysis in laboratory stick-slip experiments. *Geology*, *45*(9), 815–818. https://doi.org/10.1130/g39147.1

Goebel, T. H. W., & Shirzaei, M. (2020). More than 40 yr of potentially induced seismicity close to the san Andreas fault in san Ardo, Central California. *Seismological Research Letters*, *92*(1), 187–198. https://doi.org/10.1785/0220200276

Goebel, T. H. W., Weingarten, M., Chen, X., Haffener, J., & Brodsky, E. E. (2017b). The 2016 Mw5.1 Fairview, Oklahoma earthquakes: Evidence for long-range poroelastic triggering at >40 km from fluid disposal wells. *Earth and Planetary Science Letters*, *472*, 50–61. https://doi.org/10.1016/j.epsl.2017.05.011

Gori, M., Rubino, V., Rosakis, A. J., & Lapusta, N. (2021). Dynamic rupture initiation and propagation in a fluid-injection laboratory setup with diagnostics across multiple temporal scales. *Proceedings of the National Academy of Sciences*, *118*(51), e2023433118. https://doi.org/10.1073/pnas.2023433118

Grigoli, F., Cesca, S., Rinaldi, A. P., Manconi, A., López-Comino, J. A., Clinton, J. F., et al. (2018). The November 2017 Mw 5.5 Pohang earthquake: A possible case of induced seismicity in South Korea. *Science*, *360*(6392), 1003–0336. https://doi.org/10.1126/science.aat2010

Guérin-Marthe, S., Nielsen, S., Bird, R., Giani, S., & Di Toro, G. (2019). Earthquake nucleation size: Evidence of loading rate dependence in laboratory faults. *Journal of Geophysical Research: Solid Earth*, *124*(1), 689–708. https://doi.org/10.1029/2018JB016803

Guglielmi, Y., Cappa, F., Avouac, J.-P., Henry, P., & Elsworth, D. (2015). Seismicity triggered by fluid injection–induced aseismic slip. *Science*, *348*(6240), 1224–1226. https://doi.org/10.1126/science.aab0476

Healy, J., Rubey, W., Griggs, D., & Raleigh, C. (1968). The Denver earthquakes. *Science*, *161*(3848), 1301–1310. https://doi.org/10.1126/science.161.3848.1301

Jaeger, J. C., Cook, N. G., & Zimmerman, R. (2009). *Fundamentals of rock mechanics*. John Wiley & Sons.

Ji, Y. (2020). *Shear-flow characteristics of rock fractures and implications for injection-induced seismicity*. Ph.D. Nanyang Technological University. https://doi.org/10.32657/10356/143989

Ji, Y., Fang, Z., & Wu, W. (2021). Fluid overpressurization of rock fractures: Experimental investigation and analytical modeling. *Rock Mechanics and Rock Engineering*, *54*(6), 3039–3050. https://doi.org/10.1007/s00603-021-02453-8

Ji, Y., Hofmann, H., Duan, K., & Zang, A. (2022). Laboratory experiments on fault behavior towards better understanding of injection-induced seismicity in geoenergy systems. *Earth-Science Reviews*, *226*, 103916. https://doi.org/10.1016/j.earscirev.2021.103916

Ji, Y., Kluge, C., Hofmann, H., & Blöcher, G. (2022). Effects of external temperature and dead volume on laboratory measurements of pore pressure and injected volume in a rock fracture. *Journal of Rock Mechanics and Geotechnical Engineering*, *14*(5), 1461–1469. https://doi.org/10.1016/j.jrmge.2021.12.007

Ji, Y., Wanniarachchi, W. A. M., & Wu, W. (2020). Effect of fluid pressure heterogeneity on injection-induced fracture activation. *Computers and Geotechnics*, *123*, 103589. https://doi.org/10.1016/j.compgeo.2020.103589

Ji, Y., & Wu, W. (2020). Injection-driven fracture instability in granite: Mechanism and implications. *Tectonophysics*, *791*, 228572. https://doi.org/10.1016/j.tecto.2020.228572

Kaneko, Y., & Lapusta, N. (2008). Variability of earthquake nucleation in continuum models of rate-and-state faults and implications for aftershock rates. *Journal of Geophysical Research*, *113*(B12), B12312. https://doi.org/10.1029/2007jb005154

Kluge, C., Blöcher, G., Barnhoorn, A., & Bruhn, D. (2020). Hydraulic-mechanical properties of microfaults in granitic rock using the punch-through shear test. *International Journal of Rock Mechanics and Mining Sciences*, *134*, 104393. https://doi.org/10.1016/j.ijrmms.2020.104393

Kohli, A. H., & Zoback, M. D. (2013). Frictional properties of shale reservoir rocks. *Journal of Geophysical Research: Solid Earth*, *118*(9), 5109–5125. https://doi.org/10.1002/jgrb.50346

Kwiatek, G., Goebel, T. H. W., & Dresen, G. (2014). Seismic moment tensor and b value variations over successive seismic cycles in laboratory stick-slip experiments. *Geophysical Research Letters*, *41*(16), 5838–5846. https://doi.org/10.1002/2014gl060159

Kwiatek, G., Saarno, T., Ader, T., Bluemle, F., Bohnhoff, M., Chendorain, M., et al. (2019). Controlling fluid-induced seismicity during a 6.1-km-deep geothermal stimulation in Finland. *Science Advances*, *5*(5), eaav7224. https://doi.org/10.1126/sciadv.aav7224

Langenbruch, C., & Zoback, M. D. (2016). How will induced seismicity in Oklahoma respond to decreased saltwater injection rates? *Science Advances*, *2*(11). https://doi.org/10.1126/sciadv.1601542

Latour, S., Schubnel, A., Nielsen, S., Madariaga, R., & Vinciguerra, S. (2013). Characterization of nucleation during laboratory earthquakes. *Geophysical Research Letters*, *40*(19), 5064–5069. https://doi.org/10.1002/grl.50974

Lei, X., Huang, D., Su, J., Jiang, G., Wang, X., Wang, H., et al. (2017). Fault reactivation and earthquakes with magnitudes of up to Mw4.7 induced by shale-gas hydraulic fracturing in Sichuan Basin, China. *Scientific Reports*, *7*(1), 7971. https://doi.org/10.1038/s41598-017-08557-y

Lockner, D. A., Okubo, P. G., & Dieterich, J. H. (1982). Containment of stick-slip failures on a simulated fault by pore fluid injection. *Geophysical Research Letters*, *9*(8), 801–804. https://doi.org/10.1029/GL009i008p00801

Marone, C., Raleigh, C. B., & Scholz, C. H. (1990). Frictional behavior and constitutive modeling of simulated fault gouge. *Journal of Geophysical Research*, *95*(B5), 7007. https://doi.org/10.1029/JB095iB05p07007

McGarr, A. (2014). Maximum magnitude earthquakes induced by fluid injection. *Journal of Geophysical Research: Solid Earth*, *119*(2), 1008–1019. https://doi.org/10.1002/2013jb010597

McGarr, A., & Barbour, A. J. (2018). Injection-induced moment release can also be aseismic. *Geophysical Research Letters*, *45*(11), 5344–5351. https://doi.org/10.1029/2018GL078422

McLaskey, G. C. (2019). Earthquake initiation from laboratory observations and implications for foreshocks. *Journal of Geophysical Research: Solid Earth*, *124*(12), 12882–12904. https://doi.org/10.1029/2019jb018363

McLaskey, G. C., & Lockner, D. A. (2014). Preslip and cascade processes initiating laboratory stick slip. *Journal of Geophysical Research: Solid Earth*, *119*(8), 6323–6336. https://doi.org/10.1002/2014JB011220

McLaskey, G. C., & Yamashita, F. (2017). Slow and fast ruptures on a laboratory fault controlled by loading characteristics. *Journal of Geophysical Research: Solid Earth*, *122*(5), 3719–3738. https://doi.org/10.1002/2016jb013681

Noël, C., Passelègue, F. X., Giorgetti, C., & Violay, M. (2019). fault reactivation during fluid pressure oscillations: Transition from stable to unstable slip. *Journal of Geophysical Research: Solid Earth*, *124*(11), 10940–10953. https://doi.org/10.1029/2019jb018517

Ohnaka, M., & Shen, L.-F. (1999). Scaling of the shear rupture process from nucleation to dynamic propagation: Implications of geometric irregularity of the rupturing surfaces. *Journal of Geophysical Research*, *104*(B1), 817–844. https://doi.org/10.1029/1998jb900007

Passelègue, F. X., Almakari, M., Dublanchet, P., Barras, F., Fortin, J., & Violay, M. (2020). Initial effective stress controls the nature of earthquakes. *Nature Communications*, *11*(1), 5132. https://doi.org/10.1038/s41467-020-18937-0

Passelègue, F. X., Brantut, N., & Mitchell, T. M. (2018). Fault reactivation by fluid injection: Controls from stress state and injection rate. *Geophysical Research Letters*, *45*(23), 12–837. https://doi.org/10.1029/2018GL080470

Passelègue, F. X., Schubnel, A., Nielsen, S., Bhat, H. S., Deldicque, D., & Madariaga, R. (2016). Dynamic rupture processes inferred from laboratory microearthquakes. *Journal of Geophysical Research: Solid Earth*, *121*(6), 4343–4365. https://doi.org/10.1002/2015jb012694

Proctor, B., Lockner, D. A., Kilgore, B. D., Mitchell, T. M., & Beeler, N. M. (2020). Direct evidence for fluid pressure, dilatancy, and compaction affecting slip in isolated faults. *Geophysical Research Letters*, *47*(16), e2019GL086767. https://doi.org/10.1029/2019gl086767

Reches, Z., & Lockner, D. A. (2010). Fault weakening and earthquake instability by powder lubrication. *Nature*, *467*(7314), 452–455. https://doi.org/10.1038/nature09348

Rice, J. R. (1983). Constitutive relations for fault slip and earthquake instabilities. *PAGEOPH*, *121*(3), 443–475. https://doi.org/10.1007/BF02590151

Ross, Z. E., Meier, M. A., & Hauksson, E. (2018). P wave arrival picking and first-motion polarity determination with deep learning. *Journal of Geophysical Research: Solid Earth*, *123*(6), 5120–5129. https://doi.org/10.1029/2017jb015251

Rubin, A. M., & Ampuero, J.-P. (2005). Earthquake nucleation on (aging) rate and state faults. *Journal of Geophysical Research*, *110*(B11). https://doi.org/10.1029/2005JB003686

Rudnicki, J. W., & Zhan, Y. (2020). Effect of pressure rate on rate and state frictional slip. *Geophysical Research Letters*, *47*(21), e2020GL089426. https://doi.org/10.1029/2020GL089426

Ruina, A. (1983). Slip instability and state variable friction laws. *Journal of Geophysical Research*, *88*(B12), 10359–10370. https://doi.org/10.1029/JB088iB12p10359

Rutter, E., & Hackston, A. (2017). On the effective stress law for rock-on-rock frictional sliding, and fault slip triggered by means of fluid injection. *Philosophical Transactions of the Royal Society A: Mathematical, Physical & Engineering Sciences*, *375*(2103), 20160001. https://doi.org/10.1098/rsta.2016.0001

Sáez, A., Lecampion, B., Bhattacharya, P., & Viesca, R. C. (2022). Three-dimensional fluid-driven stable frictional ruptures. *Journal of the Mechanics and Physics of Solids*, *160*, 104754. https://doi.org/10.1016/j.jmps.2021.104754

Scholz, C. H. (2019). *The mechanics of earthquakes and faulting*. Cambridge University Press.

Stanchits, S., Mayr, S., Shapiro, S., & Dresen, G. (2011). Fracturing of porous rock induced by fluid injection. *Tectonophysics*, *503*(1–2), 129–145. https://doi.org/10.1016/j.tecto.2010.09.022

Stein, S., & Wysession, M. (2009). *An introduction to seismology, earthquakes, and earth structure*. John Wiley & Sons.

Tembe, S., Lockner, D. A., & Wong, T.-F. (2010). Effect of clay content and mineralogy on frictional sliding behavior of simulated gouges: Binary and ternary mixtures of quartz, illite, and montmorillonite. *Journal of Geophysical Research*, *115*(B3), B03416. https://doi.org/10.1029/2009jb006383

Terzaghi, K. v. (1923). Die berechnung der durchlassigkeitsziffer des tones aus dem verlauf der hydrodynamischen spannungserscheinungen. *Sitzungsberichte der Akademie der Wissenschaften in Wien, Mathematisch-Naturwissenschaftliche Klasse, Abteilung IIa*, *132*(3–4), 125–138.

Tinti, E., Scuderi, M. M., Scognamiglio, L., Di Stefano, G., Marone, C., & Collettini, C. (2018). On the evolution of elastic properties during laboratory stick-slip experiments spanning the transition from slow slip to dynamic rupture. *Journal of Geophysical Research: Solid Earth*, *121*(12), 8569–8594. https://doi.org/10.1002/2016jb013545

Wang, L., Kwiatek, G., Rybacki, E., Bohnhoff, M., & Dresen, G. (2020). Injection-induced seismic moment release and laboratory fault slip: Implications for fluid-induced seismicity. *Geophysical Research Letters*, *47*(22), e2020GL089576. https://doi.org/10.1029/2020GL089576

Wang, L., Kwiatek, G., Rybacki, E., Bonnelye, A., Bohnhoff, M., & Dresen, G. (2020). Laboratory study on fluid-induced fault slip behavior: The role of fluid pressurization rate. *Geophysical Research Letters*, *47*(6), e2019GL086627. https://doi.org/10.1029/2019gl086627

Weingarten, M., Ge, S., Godt, J. W., Bekins, B. A., & Rubinstein, J. L. (2015). High-rate injection is associated with the increase in US mid-continent seismicity. *Science*, *348*(6241), 1336–1340. https://doi.org/10.1126/science.aab1345

Xu, S., Fukuyama, E., Yamashita, F., Mizoguchi, K., Takizawa, S., & Kawakata, H. (2018). Strain rate effect on fault slip and rupture evolution: Insight from meter-scale rock friction experiments. *Tectonophysics*, *733*, 209–231. https://doi.org/10.1016/j.tecto.2017.11.039

Ye, Z., & Ghassemi, A. (2018). Injection-induced shear slip and permeability enhancement in granite fractures. *Journal of Geophysical Research: Solid Earth*, *123*(10), 9009–9032. https://doi.org/10.1029/2018JB016045

Zang, A., Oye, V., Jousset, P., Deichmann, N., Gritto, R., McGarr, A., et al. (2014). Analysis of induced seismicity in geothermal reservoirs—An overview. *Geothermics*, *52*, 6–21. https://doi.org/10.1016/j.geothermics.2014.06.005

Zoback, M. D., & Gorelick, S. M. (2012). Earthquake triggering and large-scale geologic storage of carbon dioxide. *Proceedings of the National Academy of Sciences of the United States of America*, *109*(26), 10164–10168. https://doi.org/10.1073/pnas.1202473109

References From the Supporting Information

Almakari, M., Chauris, H., Passelègue, F., Dublanchet, P., & Gesret, A. (2020). Fault's hydraulic diffusivity enhancement during injection induced fault reactivation: Application of pore pressure diffusion inversions to laboratory injection experiments. *Geophysical Journal International*, *223*(3), 2117–2132. https://doi.org/10.1093/gji/ggaa446

Brady, B. H., & Brown, E. T. (2013). *Rock mechanics: For underground mining*. Springer Science & Business Media.

Ester, M., Kriegel, H.-P., Sander, J., & Xu, X. (1996). A density-based algorithm for discovering clusters in large spatial databases with noise. In *Proceedings of the second international conference on knowledge discovery and data mining (KDD-96)* (pp. 226–231). AAAI.

Karner, S. L., & Marone, C. (2000). Effects of loading rate and normal stress on stress drop and stick-slip recurrence interval. *GeoComplexity and the Physics of Earthquakes*, *120*, 187–198. https://doi.org/10.1029/GM120p0187

Mackwell, S. J., & Paterson, M. S. (2002). New developments in deformation studies: High-strain deformation. *Reviews in Mineralogy and Geochemistry*, *51*(1), 1–19. https://doi.org/10.2138/gsrmg.51.1.1

Paglialunga, F., Passelègue, F. X., Brantut, N., Barras, F., Lebihain, M., & Violay, M. (2022). On the scale dependence in the dynamics of frictional rupture: Constant fracture energy versus size-dependent breakdown work. *Earth and Planetary Science Letters*, *584*, 117442. https://doi.org/10.1016/j.epsl.2022.117442

Shapiro, S. A., Huenges, E., & Borm, G. (1997). Estimating the crust permeability from fluid-injection-induced seismic emission at the KTB site. *Geophysical Journal International*, *131*(2), F15–F18. https://doi.org/10.1111/j.1365-246X.1997.tb01215.x

Wu, B. S., & McLaskey, G. C. (2019). Contained laboratory earthquakes ranging from slow to fast. *Journal of Geophysical Research: Solid Earth*, *124*(10), 10270–10291. https://doi.org/10.1029/2019jb017865